RSC Advances

This is an *Accepted Manuscript*, which has been through the Royal Society of Chemistry peer review process and has been accepted for publication.

Accepted Manuscripts are published online shortly after acceptance, before technical editing, formatting and proof reading. Using this free service, authors can make their results available to the community, in citable form, before we publish the edited article. This *Accepted Manuscript* will be replaced by the edited, formatted and paginated article as soon as this is available.

You can find more information about *Accepted Manuscripts* in the Information for Authors.

Please note that technical editing may introduce minor changes to the text and/or graphics, which may alter content. The journal's standard Terms & Conditions and the Ethical guidelines still apply. In no event shall the Royal Society of Chemistry be held responsible for any errors or omissions in this *Accepted Manuscript* or any consequences arising from the use of any information it contains.

ROYAL SOCIETY OF CHEMISTRY

www.rsc.org/advances

A Table of Contents Entry

RA-ART-12-2014-016494: Self-assembled Macro Porous ZnS-Graphene Aerogels for Photocatalytic Degradation of Contaminants in Water by D. A. Reddy et al.

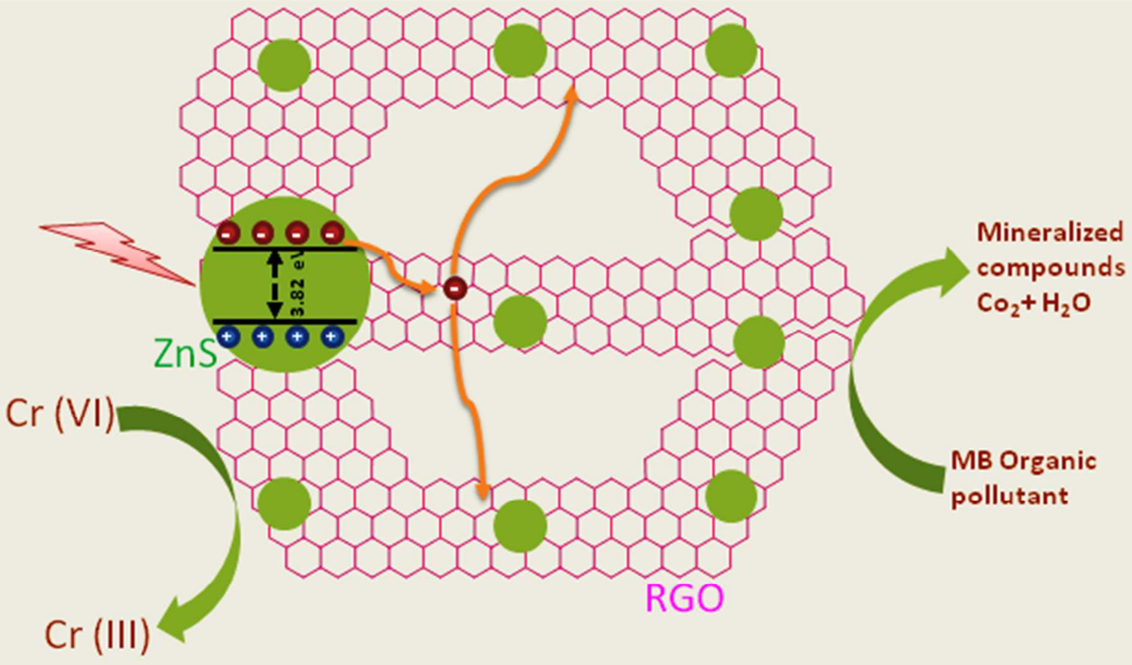

→ This work demonstrates the facile green synthesis of ZnS-graphene aerogels with superior photocatalytic performance.

RSC Advances Accepted Manuscript

Journal Name RSCPublishing

ARTICLE

Cite this: DOI: 10.1039/x0xx00000x

Received 00th January 2012,
Accepted 00th January 2012

DOI: 10.1039/x0xx00000x

www.rsc.org/

Self-assembled Macro Porous ZnS-Graphene Aerogels for Photocatalytic Degradation of Contaminants in Water

D. Amaranatha Reddy, Jiha Choi, Seunghee Lee, Rory Ma, and Tae Kyu Kim*

A facile, green protocol for synthesis of self-assembled 3D porous ZnS-graphene aerogels (ZnS-GAs) using vitamin-C to obtain a 3D network of supramolecular hybrid nanostructured materials was developed. Structural, morphological, and optical measurements demonstrate that the ZnS-GAs nanostructures have good crystallinity, and the graphene nanosheets are densely decorated by ZnS nanostructures. The photocatalytic properties of ZnS-GAs were assessed based on photocatalytic degradation of methylene blue (MB) and Cr(VI) under simulated sunlight irradiation. Superior photocatalytic performance was achieved with the ZnS-GAs compared to bare ZnS. This enhancement is ascribed to efficient charge transfer from ZnS to the graphene sheets. Overall, the present work provides new insight into the green synthesis of 3D ZnS-GAs, and the developed composites are highly active photocatalysts with stable cycling that can be exploited in environmentally friendly applications.

Introduction

Rapid industrial growth with lack of proper pollution control measures is effectively leading to environmental damage by the release of organic and inorganic pollutants into the air and water resources. This, in turn, has resulted in damage to the human ecology that is more severe than ever before. The quality of life and the eco-system are both at continuous risk due to water pollution in particular. Sustainable development of the human society is projected to require development of renewable and pollution-free technologies for environmental remediation and as alternative clean energy resources[1]. Ideally, these desired technologies should be inexpensive, environmentally friendly, and should not cause secondary pollution[1]. Among the various green technologies, semiconductor photocatalysis has gained significant interdisciplinary attention as this technique meets the criteria for addressing the current energy and environmental issues[2]. Since Fujishima and Honda first reported photocatalytic water-splitting on a TiO_2 electrode[3] under ultraviolet illumination, this technique has become a promising approach for environmentally friendly remediation of global air and water pollution. However, the applicability of TiO_2 in terms of its scope and utilization efficiency is restricted because TiO_2 is active only in the UV range, which accounts for less than 5% of sunlight. Although TiO_2 is considered as the best photocatalyst under UV radiation, the development of highly active photocatalysts under the natural sunlight or simulated sunlight irradiation still remains as a difficult task. Therefore, it is of fundamental interest to explore new types of photocatalysts that are active under sunlight irradiation as alternatives to the TiO_2 nanostructures. In this regard, several photocatalysts have recently been reported, including ZnO[4], $BiVO_4$[5], $ZnTiO_3$[6], $Bi_{12}TiO_{20}$[7], $ZnMoO_x$[8], Ag_3PO_4[9], AgCl[10], Bi_4TaO_8Cl[11], MoO_3[12], α-Fe_2O_3[13], CdS[14], AgBr[15], $SrTiO_3$[16], AgBr[17], WO_3[18], Cu_2O[19], etc.

Among the plethora of semiconductor photocatalysts, zinc sulfide (ZnS) nanostructures have aroused particular interest owing to their fascinating magnetic and optical properties. These properties make ZnS a formidable rival to TiO_2 for light emitting diode applications, spintronics, and semiconducting electronic devices[20]. In addition, ZnS has been found to be a promising photocatalyst due to the high negative reduction potentials of the excited electrons and the rapid generation of electron–hole pairs by photo-excitation processes[20]. However, ZnS suffers from some critical drawbacks, mainly associated with the difficulty involved in thorough recycling of the ZnS nanostructures after catalytic wastewater treatment, where secondary pollution may be generated by the remaining photocatalyst powder[21]. To overcome these difficulties, nanocrystals combining magnetic and catalytic activity have been developed to facilitate separation and to enhance their potential catalytic utility for practical applications. Appreciable

RSC Advances Accepted Manuscript

progress has been achieved in the production of magnetically recyclable photocatalyst materials by simply adding magnetically active materials as dopants and in the generation of magnetic core-shell nanostructures[22,23]. For instance, Anshu *et al*. reported the suitability of cobalt doped ZnS nanoparticles for recyclable photocatalysts[22], while Senapati *et al*. reported enhanced photocatalytic activity and easy magnetic separation of a $CoFe_2O_4$-ZnS composite[23]. Although the aforementioned techniques address the issue of ZnS separation after photocatalysis treatment, the limited interaction of the magnetic nanocrystals with organic pollutants and the consequently low photocatalytic performance is yet to be resolved. In this regard, self-assembled 3D graphene aerogels (GAs) decorated with semiconducting nanoparticles offer new possibilities for addressing these issues by exploiting their high specific surface area, porous structure, fast electron transport kinetics due to the continuous graphene backbone, and enhanced active sites. Moreover, by careful selection of the reaction vessel and conditions during synthesis, the volume, density, and shape of the 3D graphene aerogels can be controlled, thereby facilitating large scale production[24].

Up to now, only a few studies have focused on developing various metal and semiconductor/3D-graphene composite structures with enhanced performance relative to the individual nanostructures. For instance, Qiu *et al*.[25] observed that under sunlight irradiation, 90% degradation of methyl orange (MO) could be achieved using TiO_2-GAs. The low density and large particle size enabled facile recycling without morphological changes, with high durability of TiO_2-GAs (found to be 83% even after 5 cycles). Hou *et al*.[26] reported that the P_{25}–graphene hydrogel behaves as a high performance photocatalyst, and the maximum adsorption capacity of the hydrogel for methylene blue (MB) was as high as 87.63 mg g^{-1}. Wu *et al*.[27] reported that Cu and Cu_2O modified graphene aerogels exhibited good catalytic performance for the catalytic reduction of 4-nitrophenol and for photocatalytic degradation of methyl orange; these aerogels also exhibited excellent capacity for removing various oils and dyes from water. Li *et al*.[28] observed improved rate and cycling stability with $W_{18}O_{49}$-reduced graphene oxide (RGO) aerogels composites compared to bare $W_{18}O_{49}$ nanowires. Furthermore, the efficiency of the photocatalytic activity of the $W_{18}O_{49}$-RGO aerogel was maintained after 30 cycles. Dubey *et al*.[29] found that a graphene–carbon sphere hybrid aerogel decorated with silver nanoparticles was an efficient catalyst for the reduction of 4-nitrophenol. Similarly, novel 3D graphene aerogels such as Fe_3O_4/N-GAs[30], SnO_2/GAs[31], SnS_2/GAs[32], MnO_2/GAs[33], *etc*., were synthesized for targeted applications. Although ZnS is one of fascinating photocatalysts, to the best of our knowledge, novel ZnS-graphene aerogels with structural, optical, photoluminescent, and photocatalytic activity have not yet been reported. To fill the lacuna in the research on composite structured ZnS-graphene aerogels and their promising environmentally friendly applications, we report herein the preparation and characterization of 3D ZnS-graphene aerogel nanocomposites. The developed ZnS-GAs composite shows improved simulated sunlight driven photocatalytic degradation capacity for organic pollutants (typified by MB) and Cr(VI) compared with bare ZnS, and the free-standing nature of the composite enables facile post-treatment of water.

Experimental

Graphene oxide synthesis

Graphene oxide (GO) was prepared from natural graphite flakes according to the modified Hummers method[34]. Briefly, 69 mL of concentrated H_2SO_4 was slowly added to a mixture of graphite powder (3 g; 1 wt equiv) and $NaNO_3$ (1.5 g; 0.5 wt equiv) in a 500 mL beaker. The mixture was cooled to 0 ^oC in an ice bath and stirred for 1 h. Subsequently, $KMnO_4$ (9.0 g; 3 wt equiv) was added slowly in portions to keep the reaction temperature below 20 °C. The beaker was then placed in a 35 ^oC water bath, and the solution was stirred for about 1 h to form a thick paste, after which ultra-pure DI water (138 mL) was added slowly to produce a large exothermic heat rise to 98 ^oC; this temperature was maintained for 30 min. A mixture of DI water (420 mL) and 30% H_2O_2 (10 mL) was then added to generate another exothermic heat rise at a temperature of below 20 ^oC. Finally, the solution was filtered to collect the precipitate. The filter cake (graphite oxide) was washed (3–4 times) using HCl (30%) + DI water. The GO suspension was subsequently obtained by sonicating the as-prepared solid in water under ambient conditions for 60 min.

ZnS and ZnS-graphene aerogel synthesis

ZnS nanospheres were synthesized by a hydrothermal method. In a typical synthesis run, $Zn(CH_3COO)_2{\cdot}6H_2O$ and $SC(NH_2)_2$ were dissolved in DI water in a Teflon-lined autoclave in a 1:2 ratio based on stoichiometry. After stirring for 3 h, the autoclave was placed inside a furnace and heated at 100 ^oC for 8 h. After completion of the reaction, the autoclave was air cooled to room temperature. The products were collected and washed with DI water several times to remove the impurities and then finally heated in air at 100 ^oC for 8 h to get the final products. For the preparation of ZnS-GAs, in addition to the ZnS reducing agent, vitamin-C and GO (2 mg/mL) were also used. The as-obtained hydrogels were collected and blotted with filter paper to remove surface-adsorbed water and finally freeze-dried for complete removal of water molecules.

Characterization

The morphologies and average particle sizes were evaluated using a HITACHI S-4800 scanning electron microscope (SEM) equipped with an energy-dispersive spectrometer (EDS, Inca 400, Oxford Instruments). The microstructural properties were evaluated by using a transmission electron microscope (TEM) with an accelerating voltage of 200 kV (JEM-2100F, JEOL). Phase determination of the as-prepared powders was performed using a Bruker D8 Advance X-ray diffractometer with Cu K_α

RSC Advances Accepted Manuscript

radiation as the X-ray source. X-ray photoelectron spectroscopy (XPS) measurements were also performed with a monochromated Al K$_\alpha$ X-ray source ($h\nu$ = 1486.6 eV) at an energy of 15 kV/150 W. Raman spectra were obtained on a Nanofinder 30 micro Raman spectrometer with a solid-state laser (excitation at 487.55 nm) at room temperature in the range of 500–2500 cm^{-1}. Fourier-transform infrared (FTIR) spectra were recorded between 4000 and 500 cm^{-1} at a spectral resolution of 4 cm^{-1} (Nicolet 380). The Optical absorption measurements were performed using a UV-1800 SHIMADZU double beam spectrophotometer. In addition, PL measurements were performed at room temperature using a Hitachi F-7000 fluorescence spectrophotometer.

Photocatalytic Experiments

The photocatalytic activity of the ZnS, GAs, and ZnS-GAs nanocomposites was evaluated by calculating the percentage of dye (organic pollutant) and Cr(VI) decomposed under simulated sunlight irradiation. A solar simulator equipped with an AM 1.5 G filter and a 150-W Xe lamp (Abet Technologies) was used as a light source. During the photocatalysis experiment, the obtained photocatalyst aerogel was immersed in 100 mL of an aqueous solution of MB and Cr(VI), where the concentration (C_o) of each species was 20 mg L^{-1}. The final solution was exposed to simulated sunlight irradiation under magnetic stirring. At given time intervals of illumination, about 5 mL of the solution was withdrawn and the UV/Vis spectrum of the supernatant was recorded to monitor the adsorption and degradation behavior of each species. The characteristic intense absorption peak was monitored and compared to determine the extent of degradation of each species.

Results and Discussion

Mechanism of formation of the aerogel and the role of Vitamin-C

To obtain a supramolecular 3D network of hybrid ZnS-GAs nanostructures, vitamin-C was used as a reducing agent. The non-toxic nature of vitamin-C makes it advantageous over other reducing agents like N_2H_4, $NaBH_4$, etc. Vitamin-C also aids in the production of uniformly distributed hydrogels without the emission of toxic gases during the reduction process. The schematic experimental procedure for preparation of the ZnS-graphene aerogels is illustrated in Fig. 1(a). In performing the experiment, we noticed that two factors should be controlled in order to obtain free standing ZnS-GAs. Firstly, the concentration of the GO solution should be equal to or exceed 2.0 mg/mL, and secondly, physical disturbances should be avoided completely. Prior to reduction, GO was well dispersed in water to form a stable, aqueous, brown suspension as shown in Fig. 1(b). After adding the required stoichiometric quantity of ZnS, the color of the solution changed from brown to light black, which is indicative of the formation of ZnS nanoparticles loaded with graphene sheets. The quantitative amount of vitamin-C was mixed-in uniformly and the suspension was left undisturbed/unstirred in a muffle furnace under atmospheric pressure to obtain the ZnS-graphene hydrogels. Fig. 1(b) clearly shows that the water in which the hydrogels were suspended was completely transparent and clear, which suggests that the entire composite was self-assembled and was incorporated into the hydrogel. To elucidate the mechanism of formation of the hydrogel, the role of vitamin-C as a reducing agent should be considered. When vitamin-C is dissolved in the suspension, the vitamin-C molecules will coordinate with the graphene sheets and become attached to the surface of the graphene sheets. Preliminarily, vitamin-C acts as spacer to separate the neighboring sheets. When the precursor solution is heated, vitamin-C containing –OH and –COOH functional groups can induce GO to form interconnected and randomly oriented graphene sheets via supramolecular interactions such as hydrogen bonding, which leads to assembly of the GO sheets and final formation of the hydrogels[24]. The obtained hydrogels were freeze-dried for complete removal of water molecules and to obtain lightweight aerogels.

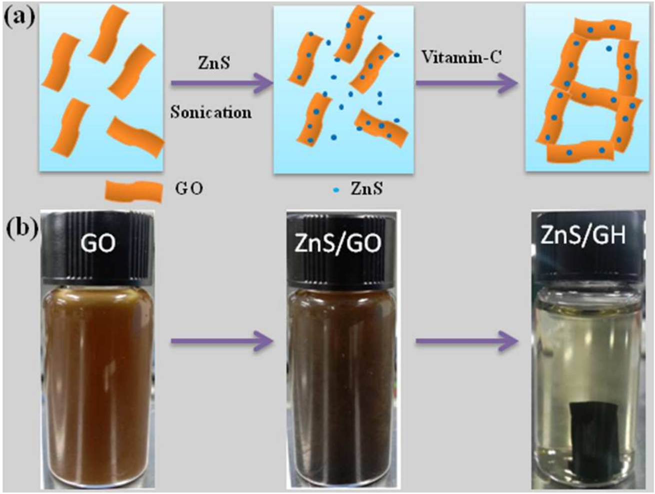

Fig. 1 (a) Schematic diagram of the mechanism of formation of ZnS-GAs. (b) Digital photos of the aqueous suspensions of graphene oxide, ZnS-GO, and ZnS-graphene hydrogel.

Morphological studies

The surface morphology of the resultant GO, GA, ZnS, and ZnS-GAs composites was characterized by FESEM as shown in Fig. 2(a)-(f). Fig. 2(a) clearly shows that isolated GO had a smooth surface morphology with an extended, ultrathin, flexible sheet-like structure. The as-prepared graphene aerogel was characterized by an interconnected, randomly oriented, 3D graphene framework with a wrinkled texture and macropores. The pores are composed of intercalated graphene sheets and the walls of the pores are thin, indicating that overlap of the graphene layers is not very extensive, as demonstrated in the FESEM images in Fig. 2(b) and (c). As-prepared ZnS had a

RSC Advances Accepted Manuscript

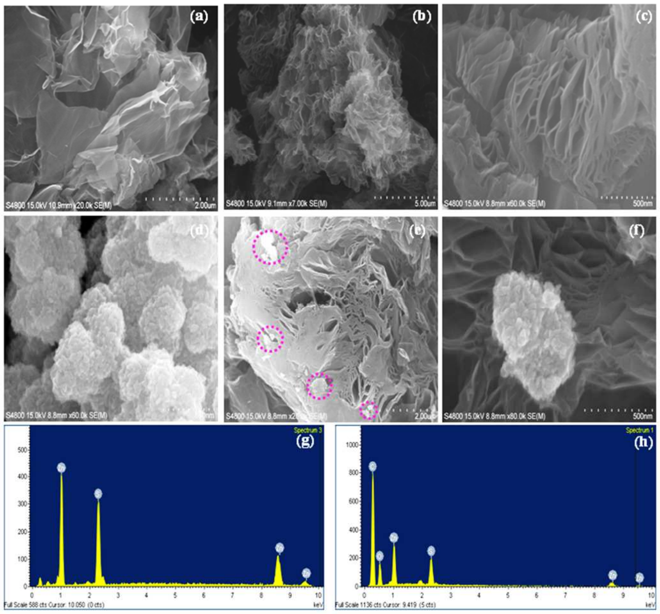

Fig. 2 FESEM images of (a) GO; (b, c) Gas; (d) ZnS; (e, f) ZnS-Gas nanocomposites. (g) and (h): EDAX spectra of ZnS and ZnS-GAS, respectively.

spheroidal and cuboidal morphology [Fig. 2(d)]. The ZnS nanoparticles were not homogeneous and their diameters ranged from 5 to 30 nm. Additionally, the surfaces of the nanostructures were rather coarse, implying that they are composed of smaller primary nanoparticles. FESEM images of the as-synthesized ZnS-GAs are shown in Fig. 2(e, f). (Additional images are shown in Fig. S1.) The images clearly shows a macroporous, interconnected, randomly oriented, 3D graphene framework with a wrinkled texture, and distribution of ZnS nanoparticles on the RGO sheets was clearly visible.

The chemical composition analysis of the ZnS and ZnS-GAs composites was performed by using the EDAX technique. Typical EDAX spectra for the as-prepared ZnS and ZnS-GAs composites are shown in Fig. 2(g) and (h), respectively. The EDAX spectra indicate the presence of Zn and S elements only in the as-prepared ZnS samples, whereas additional signals for carbon and oxygen atoms were detected for the ZnS-GAs samples.

Micro-structural analysis

Fig. 3 (a, b) TEM, (c) HRTEM, and (d) SAED patterns of ZnS-GAs nanocomposite.

The TEM, HRTEM, and SAED patterns of the ZnS-GAs nanocomposites are displayed in Fig. 3. Figs. 3(a) and (b) show the sheet-like structure of the RGO sheets with wrinkles; ZnS nanoparticles are attached to the RGO sheets. The HRTEM image [Fig. 3(c)] shows the lattice fringe, which corresponds to the (111) plane of the ZnS crystallites, in addition to the stacking layers of RGO. The fringe width was calculated to be 0.34 nm for the ZnS nanoparticles, and the stacking width was calculated to be 0.37 nm for the RGO layers. The SAED profile has a concentric ring pattern from the (111), (220), and (311) diffraction planes [Fig. 3 (d)]. Overall, the TEM, HRTEM, and SAED patterns indicate successful formation of the ZnS-GAs nanocomposite.

Structural analysis

RSC Advances Accepted Manuscript

This journal is © The Royal Society of Chemistry 2012

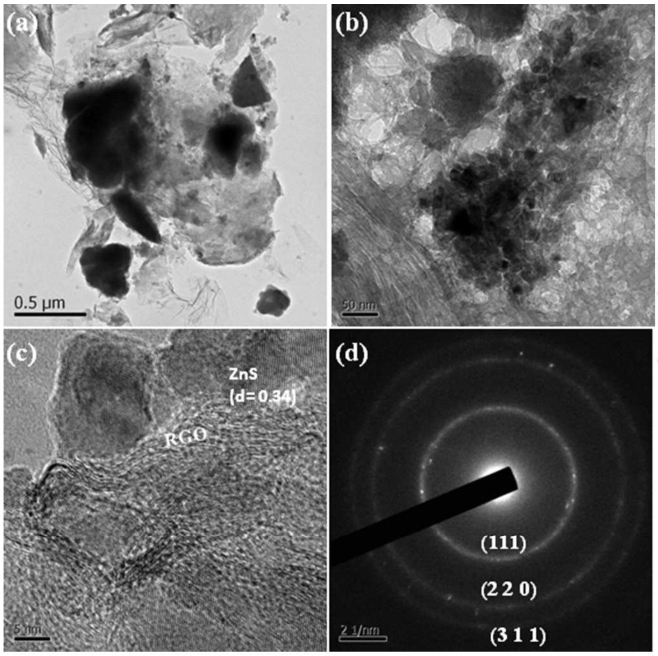

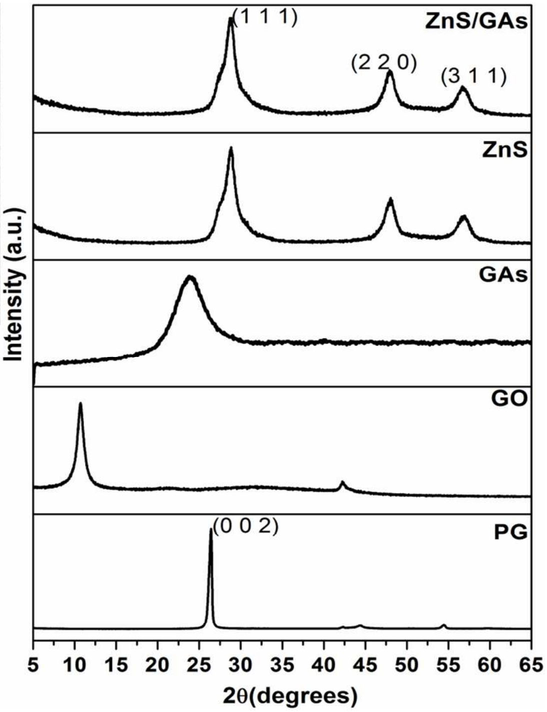

Fig. 2 X-ray diffraction (XRD) patterns of PG, GO, GA, ZnS, and ZnS-GAs

Fig. 4 shows the X-ray diffraction (XRD) patterns of pristine graphite (PG), GO, GAs, ZnS, and the ZnS-GAs nanocomposite. The results indicate significant structural differences among PG, GO, and GA. For pristine graphite, the sharp diffraction peak at 26.44°, corresponding to the (0 0 2) diffraction plane, indicates preferential growth along the c-axis with an interlayer spacing of 0.337 nm. However, for GO, the diffraction peak at 26.44° completely disappeared, and a broad diffraction peak was apparent at a lower diffraction angle ($2\theta = 10.7^{o}$), which corresponds to a *d*-spacing of 0.827 nm and suggests effective oxidation of graphite and formation of GO[35]. For the graphene aerogels, instead of the peak at $2\theta = 10.09^{o}$ for GO, a new broadened diffraction peak appeared at $2\theta = 23.77^{o}$, which is closer to the $2\theta = 26.43^{o}$ peak of graphite and corresponds to the (0 0 2) diffraction line. However, compared to that of pristine graphite, the diffraction peak was significantly broadened; this broadening indicates poor ordering of the graphene sheets along their stacking direction, and careful excogitation shows that the obtained aerogels are composed of graphene sheets stacked in few layers, which is consistent with a previous report[36]. The interlayer spacing of GA is 0.37 nm, which is slightly higher than that of pristine graphite but is much lower than that of GO. These results suggest the existence of $\pi-\pi$ stacking between the graphene sheets in the graphene aerogel and an inhomogeneous graphite-like carbon crystalline state[37]. The XRD peaks of bare ZnS and ZnS-GAs were considerably broadened due to the very small size of the particles. Three diffraction peaks were observed in the profiles of bare ZnS and ZnS-GAs at $2\theta \approx 28.8^{o}$, 48.1^{o}, and 56.9^{o}, assigned to the (1 1 1), (2 2 0), and (3 1 1) reflections of the cubic structure; all three diffraction peaks could be perfectly indexed to cubic ZnS (JCPDS 80-0020). No additional peaks were observed corresponding to S or Zn clusters, which indicates that the synthesized nano-products have high purity. The average nanocrystallite size was calculated from the full width at half maximum (FWHM) intensity of the XRD peaks using Debye–Scherrer's formula, ($D = 0.89\lambda / \beta\cos\theta$) where D is the average particle size, λ the wavelength of Cu K_{α} radiation, β the FWHM intensity of the diffraction peak, and θ the diffraction angle for the (1 1 1) plane of cubic ZnS. From the XRD analysis, the measured average crystallite sizes were in the range of 4 – 5 nm.

Fig. 5 ((a) and (c)) XPS survey spectrum of GO and ZnS-GAs nanocomposite, respectively. ((b) and (d)) narrow scan C 1*s* spectrum of GO and ZnS-GAs nanocomposite, respectively. ((e) and (f)) narrow scan Zn 2*p* and S 2*p* spectra of ZnS-GAs nanocomposite, respectively.

XPS analysis

RSC Advances Accepted Manuscript

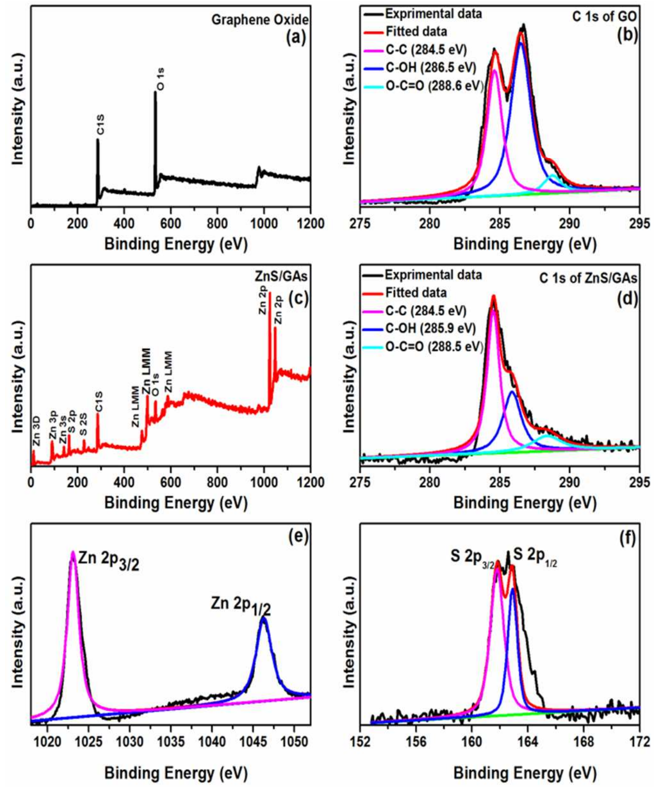

Surface compositional and elemental analyses of GO and ZnS-GAs were performed by the XPS technique. Fig. 5(a) shows the XPS spectrum of as-prepared GO, where only peaks assignable to C and O are observed. The narrow scan XPS spectrum of the C 1s peak of GO is shown in Fig. 5(b). This peak could be resolved into three Gaussian peaks centered at 284.5, 286.5 eV, and 288.6 eV. The peak at 284.5 eV is attributed to the sp^2 carbon atom, while the peak positioned at 286.5 eV is assigned to C from the C–OH and C=O groups. The peak located at 288.6 eV is closely associated with the O=C–OH carboxylic group[28]. The XPS spectrum of the ZnS-GAs sample (Fig. 5(c)) shows Zn, S, C, and O signal peaks at their respective standard binding energies, related to an environment of zinc sulfide. The above results provide strong evidence for the formation of the ZnS-GAs composite; furthermore, the C 1*s* deconvolution spectrum shown in Fig. 5(d) demonstrates three different peaks centered at 284.5, 285.9 eV, and 288.5 eV, corresponding to C–C, C–OH, and O=C–OH groups, respectively. In comparison with the GO spectrum, the intensities of these peaks were obviously reduced, indicating that GO was reduced to graphene with a small amount of residual oxygen-containing groups. Fig. 5(e) shows the high-resolution XPS spectrum of Zn 3*d*. The two strong peaks at around 1022.9 eV and 1046.2 eV can be attributed to Zn $2p_{3/2}$ and $2p_{1/2}$, respectively, which is characteristic of Zn^{2+} in the ZnS-GAs composite. Fig. 5(f) shows a representative S-core level XPS spectrum with two peaks centered at 161.8 and 162.9 eV for S $2p_{3/2}$ and $2p_{1/2}$, respectively, which is characteristic of S^{2-} in the ZnS-GAs composite[38]. The above results confirm formation of the ZnS-GAs composite.

Raman analysis

Fig. 6 shows the Raman spectra of GO, GAs, and the ZnS-GAs composite. Two major prominent bands of GO are found at 1355 and 1595 cm^{-1}, corresponding to the D and G bands of graphene, respectively. The D peak arises from disruption of the symmetrical hexagonal graphitic lattice as a result of internal structural defects, edge defects, and dangling bonds. The G band is related to the E_{2g} mode of phonon vibrations within sp^2-bonded carbon materials[39]. In the Raman spectrum of the GAs and ZnS-GAs nanostructures, the D band at 1340 cm^{-1} became prominent, indicative of destruction of the sp^2 character and the formation of defects in the sheets due to extensive oxidation. Generally, the intensity ratio of the D and G bands $I(D)/I(G)$ can be used to estimate the degree of disorder and average size of the sp^2 domains of graphite materials. It was observed that compared with GO, the $I(D)/I(G)$ ratio of GAs and ZnS-GAs increased slightly from 0.94 (GO) to 1.03 (GAs) and 1.05 (ZnS-GAs), which suggests that GO was reduced and more defects were doped into the ZnS-GAs composites.

Fig. 6 Raman spectra of GO, GAs, and ZnS-GAs nanocomposites.

FTIR analysis

FTIR spectroscopy was employed to investigate the functionalization and reduction processes. The FTIR spectra of pure GO, GAs, and the ZnS-GAs nanocomposite in the wavelength range of 4000 to 400 cm^{-1} are shown in Fig. 7. The strong and broad absorption peak at ~3396 cm^{-1} in the spectrum of GO is attributed to the O–H stretching vibrations. The spectral bands at ~1735 cm^{-1} and ~1391 cm^{-1} are assigned to the characteristic stretching vibrations of carboxyl –C=O and –C–O, respectively. The peak at ~1630 cm^{-1} is related to aromatic –C=C. The peaks at ~1225 cm^{-1} (epoxy –C–O) and ~1054 (alkoxy –C–O) indicate the presence of oxygen-containing functional groups on the GO nanosheets[39]. The peak intensity of the carbonyl group at ~1733 cm^{-1} in the spectrum of the graphene aerogel decreased markedly compared with that of GO. Moreover, the peak of the epoxy group at ~1225 cm^{-1} almost disappeared in the spectrum of the graphene aerogel, which implies efficient reduction of GO and subsequent assembly of the graphene sheets into 3D structures due to reduction of the hydroxyl groups by vitamin-C. For the ZnS-GAs composite,

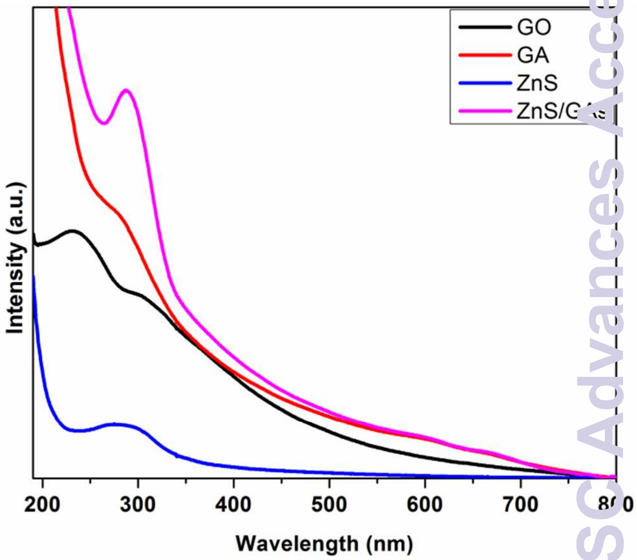

RSC Advances Accepted Manuscript

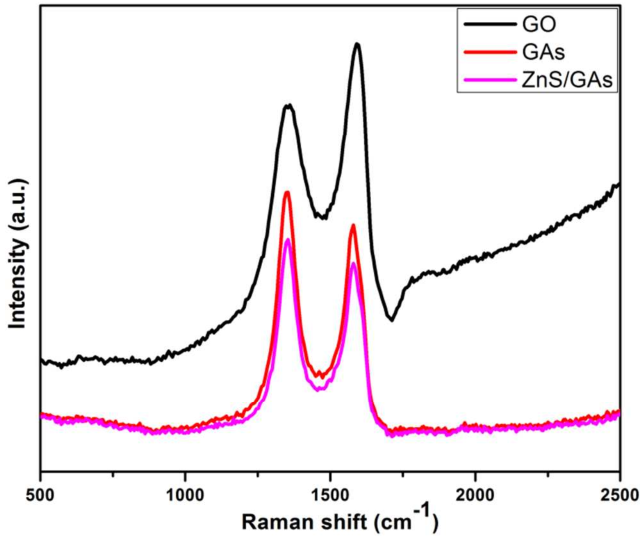

Fig. 7 FTIR spectra of GO, GAs, and ZnS-GAs nanocomposite.

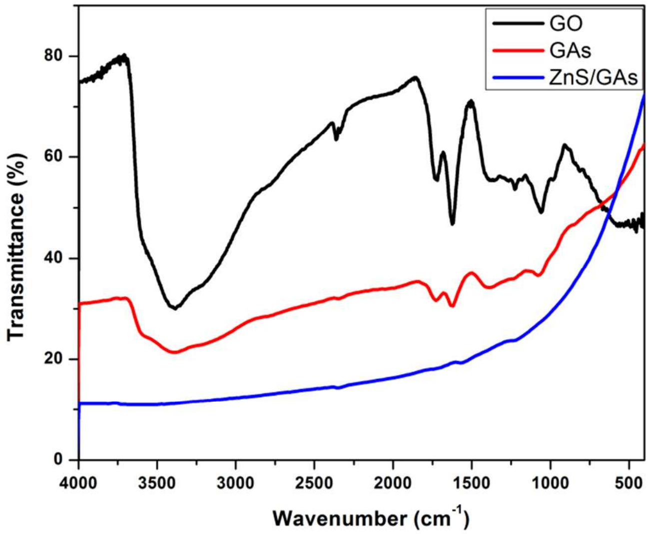

only a skeletal vibration peak at around 1500 cm^{-1} was observed in the FTIR spectrum, indicating the formation of graphene.

Optical absorption studies

The UV–visible absorbance spectra of the as-synthesized GO, GA, ZnS, and ZnS-GA composites are presented in Fig. 8. A two band absorption spectrum was observed for the GO solution, having maxima at 235 and 304 nm, respectively. The bands are assigned to the $\pi - \pi^*$ transition of the aromatic C-C and C=C bonds and the $n - \pi^*$ transition of the carbonyl functional group[40]. The absorption peak of GA corresponding to the $\pi - \pi^*$ transition of the aromatic C–C bond was shifted to longer wavelength (278 nm), indicating the reduction of GO and restoration of the C-C bonds in the GA sheets[40]. The spectrum of the pure ZnS nanospheres shows an absorption edge that corresponds to a bandgap of 3.82 eV. The obtained bandgap is higher than that of bulk ZnS (bandgap of 3.6 eV), which can be ascribed to the quantum confinement effect due to the small size of the particles[41]. Compared with the absorbance of pure ZnS, the intensity of the absorbance of the ZnS-GAs composites was significantly enhanced. This increased absorbance may be due to the absorption contribution from the graphene sheets and modification of the fundamental process of exciton formation upon irradiation. Moreover, the absorption maxima shifted slightly to the higher wavelength region (red shift), indicating an appreciable decrease in the bandgap. These phenomena suggest strong coupling between the graphene sheets and ZnS. These interactions may play a significant role in improving the separation of the photogenerated electron–hole pairs to enhance the photocatalytic activity.

Photoluminescence studies

The room temperature photoluminescence (PL) spectra of ZnS and the ZnS-GAs nanocomposite with 290 nm excitation are shown in Fig. 9. A broad band ranging from 350 nm to 500 nm was observed in the PL spectra of all of the synthesized nanostructures. However, further examination revealed that both samples exhibited a broad and strong emission band with a maximum intensity centered at 408 nm, along with a violet emission shoulder at around 375 nm. The origin of the emission can be ascribed to a self-activated center, presumably formed between a Zn vacancy and a shallow donor associated with a sulfur vacancy. Previous studies[42,43] have also reported similar blue emission from ZnS nanoparticles. The present nanostructures may reasonably possess a high density of urface defects considering the small-particle-like morphology over the grown nanostructures, which is generally associated with a large surface area and is prone to a high density of surface defects. Furthermore, the misshapen, smaller, budding nanocrystals might also constitute surface defects. Overall, the presence of a high density of surface defects in the prepared nanostructures accounts for the maximum intensity blue emission. In the case of the ZnS-GAs nanocomposites, the intensity of the luminescence is quenched by as much as an order of magnitude, suggesting an additional pathway for inactivation of charge carriers due to interaction between the excited ZnS nanostructures and graphene nanosheets[43].

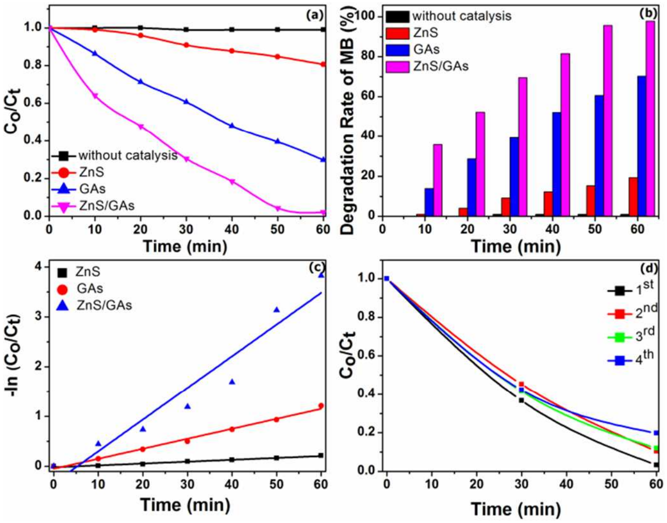

Fig. 8 UV-visible spectra of GO, GAs, and ZnS-GAs nanocomposite.

RSC Advances Accepted Manuscript

Photocatalytic activity and stability

Photocatalytic oxidation of MB

Degradation of MB was carried out in order to investigate the photocatalytic performance of bare ZnS, GAs, and the ZnS-GAs composite under sunlight irradiation; the corresponding degradation ratios (C/C_0) and degradation efficiency as a function of time are presented in Fig. 10(a) and (b), respectively. In the absence of the photocatalyst, the concentration of MB was marginally reduced. This indicates that the degradation of MB was negligible upon sunlight illumination in the absence of the photocatalyst. In the presence of bare ZnS, the MB concentration decreased so slowly that after a time span of 60 minutes, only 19.38% MB degradation was achieved. Because pure ZnS does not absorb significantly in the visible region, the observed low degradation is due to self-sensitization of the MB molecules, which extended the absorption of ZnS into the visible light region. Based on the mechanism of dye sensitization, electrons from the excited dye molecules that are adsorbed on the surface of the ZnS photocatalyst may be injected into the conduction band of the latter and thereby produce radicals. The generated radicals subsequently initiate the dye degradation process[44]. Moreover, UV-light accounts from the simulator also contribute for the degradation of MB, when ZnS nano photocatalysts are irradiated by simulated sunlight, ZnS nanostructures utilize the UV-light accounts from the simulator. When the nanostructures were irradiated, the electrons in the VB of ZnS were excited to the CB, leaving holes in the VB. The conduction band electrons took part in a reduction reaction with electron acceptors, such as adsorbed O_2 molecules, which yielded superoxide radical anions ($\cdot O_2^-$). Finally, the photo-induced holes could either oxidize the organic compound directly, or they could be trapped by electron donors, such as OH^- to produce $\cdot OH$. The superoxide radical anion and hydroxyl radicals were responsible for the decomposition of the MB dye into non-toxic products[45].

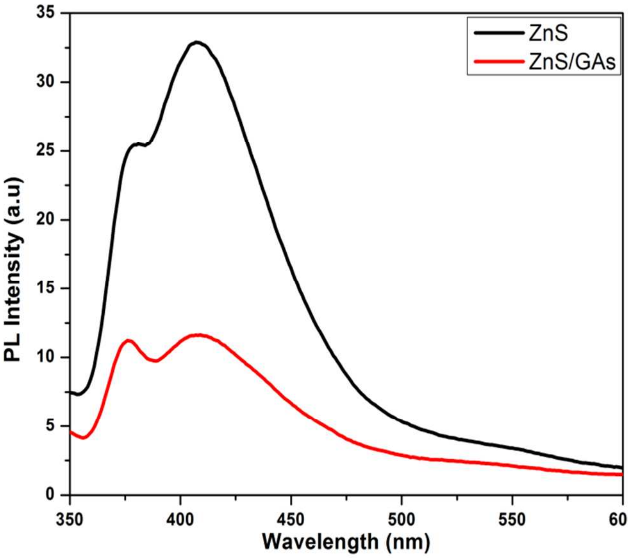

Fig. 9 Room temperature PL of ZnS and ZnS-GAs nanocomposite.

An appreciable degree of photocatalytic activity was observed for the ZnS-GAs composites based on degradation of MB. Complete degradation was achieved within 60 min, which is far superior to the degradation achieved with ZnS alone. A suitable explanation for the enhanced photocatalytic performance of ZnS-GAs involves the formation of holes in the valence band (VB) and electrons in the conduction band (CB) of the ZnS semiconductor upon irradiation with sunlight (Eq. 1). The photo-generated electrons from the ZnS nanoparticles can be transported by the RGO sheets (Eq. 2) and eventually react with absorbed molecular oxygen O_2 to generate the superoxide radical anion $\cdot O_2^-$ (Eq. 3). In aqueous medium, the photogenerated hole in the VB of ZnS can be easily trapped by the hydroxyl ion present in the solution by producing extremely strong oxidant radicals, $\cdot OH$ (Eq. 4). These oxidant radicals can recombine to form H_2O_2 (Eq. 5). H_2O_2 may then react with the superoxide radical anion to regenerate a hydroxyl radical (Eq. 6). All of the photo-generated active species can react with the adsorbed MB dye, with consequent degradation into intermediate small molecules, such as carbon dioxide and water (Eq. 7), which enhances the photocatalytic performance. The reactions representing the degradation mechanism are as follows:

Fig. 10 (a) Photocatalytic degradation of methylene blue (MB) over ZnS, GAs, and ZnS–GAs composites under solar irradiation, and in the absence of catalysts. (b) Degradation efficiency of ZnS, GAs, and ZnS–GAs composites in the photodegradation of MB as a function of time. (c) A plot of –ln(C_0/C_t) as a function of solar irradiation time for photocatalysis of MB solution containing ZnS, GAs, and ZnS–GAs composites. (d) The reusability of the ZnS-GAs composite in the

$$\mathrm{ZnS} + h\nu \longrightarrow \mathrm{ZnS}(e^-) + \mathrm{ZnS}(h^+) \tag{1}$$

$$\mathrm{ZnS}(e^-) \longrightarrow \mathrm{GO}(e^-) \tag{2}$$

$$\mathrm{GO}(e^-) + \mathrm{O_2} \longrightarrow \cdot\mathrm{O_2}^- \tag{3}$$

$$\mathrm{ZnS}(h^+) + \mathrm{H_2O} \longrightarrow \cdot\mathrm{OH} \tag{4}$$

$$\cdot\mathrm{OH} + \cdot\mathrm{OH} \longrightarrow \mathrm{H_2O_2} \tag{5}$$

$$\mathrm{H_2O_2} + \cdot\mathrm{O_2}^- \longrightarrow \mathrm{OH}^- + \cdot\mathrm{OH} + \mathrm{O_2} \tag{6}$$

$$\cdot\mathrm{OH} + \mathrm{MB} \longrightarrow \mathrm{H_2O} + \mathrm{CO_2} + \text{Mineral Acids} \tag{7}$$

During this process, the macroporous RGO nanosheets play an important role in enhancing the photocatalytic activity. Due to the high electron mobility of the RGO nanosheets, the nanosheets work as an electron collector and high speed charge transfer channel to efficiently hinder electron–hole recombination for the sustained lifetime of the photo-generated charge carriers from the ZnS nanoparticles. Therefore, the production of $\cdot OH$ and $\cdot O_2^-$ species under photo-irradiation may increase, leading to the higher photocatalytic efficiency of the ZnS-GAs photocatalysts[46].

Fig. 10(c) shows the pseudo-first order kinetics plots for MB degradation in the presence of the ZnS, GAs, and ZnS-GAs photocatalysts. The kinetics model is expressed as $-\ln(C/C_0) = kt$, where k is the apparent reaction constant, C_0 is the initial

RSC Advances Accepted Manuscript

concentration of MB, and C is the concentration of MB at different reaction times. The k value could be determined by a linear fit of the plot of $-\ln\left(C/C_0\right)$ versus reaction time t, and was found to be 0.003 min^{-1}, 0.017 min^{-1}, and 0.052 min^{-1} for ZnS, GAs, and ZnS-GAs, respectively. The highest photocatalytic performance was achieved with the ZnS-GAs nanocomposite, where k was *ca*. 17 times higher than that of pure ZnS. This result revealed that combination of RGO and ZnS effectively enhanced the photocatalytic activity under photo-irradiation.

The stability of a photocatalyst is important for practical applications, thus, the ZnS-GAs nanocomposite photocatalyst was recycled in MB degradation tests under the same conditions over 4 cycles of 60 min each as shown in Fig. 10(d). The photocatalytic efficiency of the ZnS-GAs nanocomposites did not decline significantly, which suggests that the catalysts had good stability and sustainability. Fig. S2 presents the XRD patterns of the ZnS-GAs sample before and after four runs under the simulated sunlight irradiation for the degradation of MB. It can be clearly observed that the phase and structure of the ZnS-GAs composite remained to be unchanged after photocatalytic cycles; suggesting the sample is stable under the present photocatalytic degradation process. In addition, the photocatalytic structural stabilities and photocatalytic loss of ZnS-GAs nanocomposites were investigated by XPS spectra and are shown in Fig. S3 ((a)-(d)). From the spectra it is clear that the binding energies of Zn 2p and S 2p of the recycled ZnS-GAs shows no peak- shift compared to those of the fresh sample, inferring that the chemical states of Zn and S elements in ZnS-GAs did not change during the reaction process. Moreover, Rietveld refinements reveal that the ZnS-GAs nanocomposites presented 93.85% of ZnS phase after four photocatalytic degradations, which suggests that the catalysts show good stability.

Photocatalytic reduction of Cr(VI)

The photocatalytic activity of the ZnS, GAs, and ZnS-GAs composites was also investigated in terms of the photocatalytic reduction of the Cr(VI) solution under solar irradiation. The photocatalytic reduction ratio $\left(C/C_0\right)$ and reduction efficiency as a function of time are presented in Figs. 11(a) and (b). The blank experiment in the absence of a photocatalyst shows that the self-photocatalysis reduction of Cr(VI) under simulated sunlight irradiation could be neglected. Bare ZnS exhibited very low photocatalytic activity and only 18.6% of Cr(VI) was reduced after irradiation for a time period of 60 min. The observed reduction may be explained as follows, when ZnS photocatalyst is exposed to simulated sunlight irradiation, ZnS nanostructures utilize UV-light accounts from the simulator and excitation of electrons occurs from its valence band to conduction band. This leads to generation of photoexcited electrons at its conduction band and holes in its valence band. The photoexcited electrons (e^-) are utilized for reduction of Cr(VI) to Cr(III), while at the same time the holes (h^+) oxidize water molecules to O_2 in its valence band[45].

However, in the presence of ZnS-GAs, the reduction ratio of Cr(VI) increased to 61.2% over 60 min. The enhanced photocatalytic activity of the ZnS-GAs composites can be attributed to the high specific surface area and reduction of the electron–hole pair recombination due to the introduction of GO. The mechanism of Cr(VI) reduction may be explained as follows. The photogenerated electrons (e^-) and holes (h^+) are produced upon suitable irradiation of ZnS. The photogenerated electrons reduced $Cr_2O_7^{2-}$ to Cr(III); concomitantly, the holes oxidized water to O_2 (Eqs. 8 and 9)[47].

$$Cr_2O_7^{2-} + 14H^+ + 6e^- \longrightarrow 2Cr^{3+} + 7H_2O \qquad (8)$$

$$2H_2O + 4h^+ \longrightarrow O_2 + 4H^+ \qquad (9)$$

The rate of photocatalytic reduction of the nanocomposites can be described by pseudo-first-order kinetics (Fig. 11c). The curves of $-\ln\left(C/C_0\right)$ versus irradiation time were linear, indicative of good correlation to first-order kinetics. The k for the ZnS-GAs sample was 0.0157 min^{-1}, which was 6.8 times higher than that of bare ZnS (0.0023 min^{-1}). To verify the practical applicability of the ZnS-GAs hybrid material, the reusability was further evaluated in the reduction of Cr(VI) under the same conditions over 4 photocatalytic cycles. Fig. 11(d) demonstrates that the photocatalytic activity did not

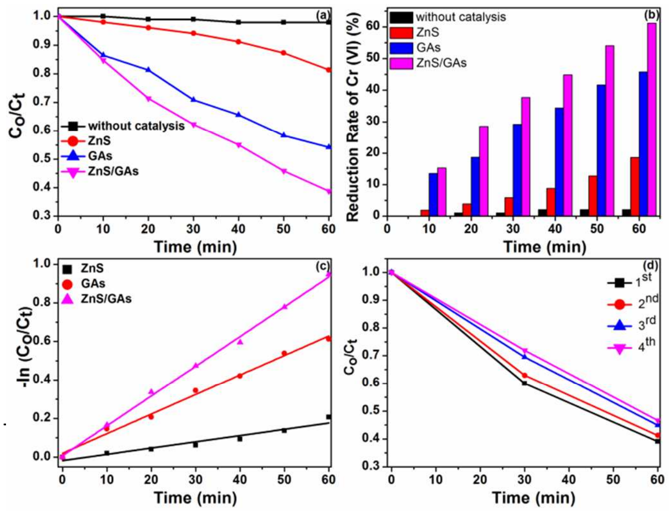

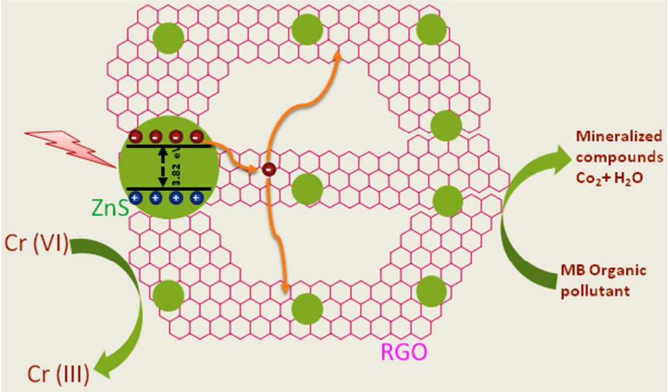

Fig. 13 Schematic diagram of bandgap matching and flow of photo-induced electrons in ZnS-GAs under simulated sunlight irradiation.

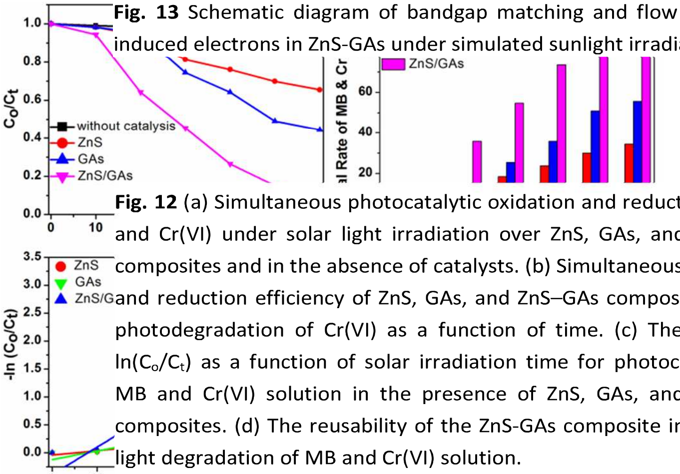

Fig. 12 (a) Simultaneous photocatalytic oxidation and reduction of MB and Cr(VI) under solar light irradiation over ZnS, GAs, and ZnS–GAs composites and in the absence of catalysts. (b) Simultaneous oxidation and reduction efficiency of ZnS, GAs, and ZnS–GAs composites in the photodegradation of Cr(VI) as a function of time. (c) The plot of -ln(C_o/C_t) as a function of solar irradiation time for photocatalysis of MB and Cr(VI) solution in the presence of ZnS, GAs, and ZnS–GAs composites. (d) The reusability of the ZnS-GAs composite in the solar light degradation of MB and Cr(VI) solution.

RSC Advances Accepted Manuscript

decline after four cycles. This indicates that stable and efficient performance of the ZnS-GAs nanocomposites was maintained during Cr(VI) reduction, which makes the photocatalyst potentially applicable for water treatment.

Simultaneous oxidation of MB and reduction of Cr(VI)

The simultaneous photocatalytic oxidation and reduction of a mixed aqueous solution containing MB and Cr(VI) in the presence of ZnS, GAs, and the ZnS-GAs nanocomposite was studied. As shown in Fig. 12(a, b), the photocatalytic reduction of Cr(VI) was more efficient in the Cr(VI)–MB dye system than in the isolated Cr(VI) system. The fast reduction rate may be due to oxidation of the MB dye via prompt and efficient consumption of the photo-excited holes, which in turn attenuates electron–hole recombination and promotes photocatalytic Cr(VI) reduction[45]. Thus, simultaneous reduction of Cr(VI) and oxidation of organic dyes on ZnS-GAs is facilitated without the use of additives due to the synchronized actions of Cr(VI) as an electron acceptor and the organic dye as an electron donor. Notably, the ZnS-GAs nanocomposite exhibits significantly enhanced activity relative to bare ZnS, and the reduction ratio increased rapidly within 60 min of sunlight illumination. The high activity of ZnS-GAs can be ascribed to the intimate interfacial contact between the graphene sheets and ZnS, leading to efficient charge separation. A plausible working mechanism for reduction of Cr^{6+} to Cr^{3+} with concomitant oxidation of MB to mineralized compounds, CO_2, and H_2O over ZnS-GAs under sunlight irradiation is shown in Fig. 13. The calculated k value for the as-prepared ZnS-GAs nanostructures was 0.0847 min^{-1} [Fig. 12(c)], which is 15.6 times higher than that of bare ZnS (0.00514 min^{-1}). This result further highlights the high photocatalytic activity of the ZnS-GAs composite catalyst under simulated sunlight irradiation. To evaluate the reusability of the ZnS-GAs composite, four successive photocatalytic experiments were carried out using an aqueous solution containing MB and Cr(VI) under simulated sunlight irradiation; the experimental results are shown in Fig. 12(d). After 4 cycles, the performance of ZnS-GAs was 90.2% of the original value, indicating the high stability and durability of the obtained nanocomposite.

Conclusions

ZnS-graphene aerogels were successfully prepared using vitamin-C as a potentially eco-friendly reducing agent. EDS, SEM, TEM, XPS, Raman, FTIR, and XRD analyses demonstrated incorporation of fine ZnS particles on the surface of the graphene sheets without formation of metallic clusters or occluded precipitates on the surface of the graphene aerogels. In addition, the feasibility of the as-prepared ZnS-GAs composite as a blue light emitting nanophosphor for fabricating near UV-white LEDs was demonstrated. The enhanced photocatalytic activity and stability of the developed ZnS-GAs composite hold promise for its utilization as a modern photocatalyst for environmentally friendly applications.

Acknowledgements

This work was financially supported by National Research Foundation of Korea (NRF) grants funded by the Korean government (MEST and MSIP) (2007-0056095, NRF-2013S1A2A2035406, NRF-2013R1A1A2009575, and 2014R1A4A1001690).

Notes and References

Department of Chemistry and Chemical Institute for Functional Materials, Pusan National University, Busan 609-735, Republic of Korea.
*Corresponding author. E-mail: tkkim@pusan.ac.kr.

Electronic Supplementary Information (ESI) available: Additional figures as mentioned in the text. See DOI: 10.1039/b000000x/

[1] V. K. Gupta, I. Ali, T. A. Saleh, A. Nayak, S. Agarwal, RSC Adv., 2012, 2, 6380–6388.
[2] D. Ravelli, D. Dondi, M. Fagnoni and A. Albini, Chem. Soc. Rev., 2009, 38, 1999–2011.
[3] A. Fujishima, K. Honda, Nature, 1972, 238, 37-38.
[4] G. Madhusudana, P. S. Kumar, D. P. Kumar, V. V. S. S. Srikanth, M. V. Shankar, Mater. Lett., 2014, 128, 183–186.
[5] M. Ge, L. Liu,W. Chen, Z. Zhou, CrystEngComm, 2012, 14, 1038-1044.
[6] T. Surendar, S. Kumar, V. Shanker, Phys. Chem. Chem. Phys., 2014, 16, 728-735.
[7] W. Guo, S. Zhang, Y. Guo, L. Ma, F. Su, Y. Guo, A. Geng, RSC Adv., 2013, 3, 4008–4017.
[8] S. Dong, L. Hu, J. Feng, Y. Pi, Q. Li, Y. Li, M. Liu, J. Sun, J. Sun, RSC Adv., 2014, 4, 64994–65003.
[9] T. L. R. Hewer, B. C. Machado, R. S. Freire, R. Guardani, RSC Adv., 2014, 4, 34674–34680.
[10] C. An, R. Wang, S. Wang, X. Zhang, J. Mater. Chem., 2011, 21, 11532–11536.
[11] S.S.M. Bhat, N.G. Sundaram, RSC Adv., 2013, 3, 14371–14378.
[12] I. Shakir, J. H. Choi, M. Shahid, Z. Alia, D. J. Kang, J. Mater. Chem., 2012, 22, 20549–20553.
[13] G.K. Pradhan, N. Sahu, K. M. Parida, RSC Adv., 2013, 3, 7912–7920.
[14] M. Kaur, C. M. Nagaraja, RSC Adv., 2014, 4, 18257–18263.
[15] J. Song, I. Lee, J. Roh, J. Jang, RSC Adv., 2014, 4, 4558–4563.
[16] S. Kumar, T. Surendar, A. Baruah, B. Kumar,V. Shanker, Dalton Trans., 2014, 43, 16105–16114.
[17] J. Song, I. Lee, J. Roh, J. Jang, RSC Adv., 2014, 4, 4558–4563.
[18] W. Mu, X. Xie, X. Li, R. Zhang, Q. Yu, K. Lv, H. Wei, Y. Jian, RSC Adv., 2014, 4, 36064–36070.
[19] T. Kou, C. Jin, C. Zhang, J. Sun, Z. Zhang, RSC Adv., 2012, 2, 12636–12643.

RSC Advances Accepted Manuscript

This journal is © The Royal Society of Chemistry 2012

[20] X. Fang, T. Zhai, U. K. Gautam, L. Li, L. Wu, Y. Bando, D. Golberg, Prog. Mater. Sci., 2011, 56, 175–287.

[21] D. Chen, F. Huang, G. Ren, D. Li, M. Zheng, Y. Wang, Z. Lin, Nanoscale, 2010, 2, 2062–2064.

[22] D. Anshu, P. Vijay, S. L. Gupta, K. S. Rathore, J. Mol. Catal., 2013, 373, 61–71.

[23] K. K. Senapati, C. Borgohain, P. Prodeep, Catal. Sci. Technol., 2012, 2, 2361–2366.

[24] W. Chena, L. Yan, Nanoscale, 2011, 3, 3132-3137.

[25] B. Qiu, M. Xing, J. Zhang, J. Am. Chem. Soc., 2014, 136, 5852–5855.

[26] C. Hou, Q. Zhang, Y. Li, H. Wang, J. Hazard. Mater., 2012, 205, 229–235.

[27] T. Wu, M. Chen, L. Zhang, X. Xu, Y. Liu, J. Yan, W. Wang, J. Gao, J. Mater. Chem. A, 2013, 1, 7612–7621.

[28] X. Li, S. Yang, J. Sun, P. He, X. Xu, G. Ding, Carbon 2014, 78, 38–48.

[29] D. S. Prabha, D. A. Dhar, I. C. Kim, M. Sillanpaa, Y. N. Kwon, C. Lee, Chem. Eng. J., 2014, 244, 160–167.

[30] Z. S. Wu, S. Yang, Y. Sun, K. Parvez, X. Feng, K. Mullen, J. Am. Chem. Soc., 2012, 134, 9082−9085.

[31] X. Liu, J. Cui, J. Sun, X. Zhang, RSC Adv., 2014, 4, 22601–22605.

[32] X. Jiang, X. Yang, Y. Zhu, J. Shen, K. Fan, C. Li, J. Power Sources, 2013, 237, 178–186.

[33] X. Zhu, P. Zhang, S. Xu, X. Yan, Q. Xue, ACS Appl. Mater. Interfaces, 2014, 6, 11665−11674.

[34] D. C. Marcano, D. V. Kosynkin, J. M. Berlin, A. Sinitskii, Z. Sun, A. Slesarev, L. B. Alemany, W. Lu, J. M. Tour, ACS Nano, 2010, 4, 4806–4814.

[35] Y. Xu, K. Sheng, C. Li, G. Shi, ACS Nano, 2010, 4, 4324–4330.

[36] Z. Zhao, X. Wang, J. Qiu, J. Lin, D. Xu, Rev. Adv. Mater. Sci. 36 (2014) 137-151.

[37] X. Zhang, Z. Sui, B. Xu, S. Yue, Y. Luo, W. Zhan, B. Liu, J. Mater. Chem., 2011, 21, 6494–6497.

[38] D. A. Reddy, D. H. Kim, S. J. Rhee, C. U. Jung, B. W. Lee, C. Liu, J. Alloys Compd., 2014, 588, 596–604.

[39] D. A. Reddy, R. Ma, M. Y. Choi, T. K. Kim, Appl. Surf. Sci., 2015, 324, 725–735.

[40] Y. Zhang, H.L. Ma, Q. Zhang, J. Peng, J. Li, M. Zhai, Z.Z. Yu, J. Mater. Chem., 2012, 22, 13064–13069.

[41] D. A. Reddy, S. Sambasivam, G. Murali, B. Poornaprakash, R. P. Vijayalakshmi, Y. Aparna, B. K. Reddy, J. L. Rao, J. Alloys Compd., 2012, 537, 208–215.

[42] D. A. Reddy, G. Murali, R. P. Vijayalakshmi, B. K. Reddy, B. Sreedhar, Cryst. Res. Technol., 2011, 46, 731–736.

[43] M. Sookhakian, Y. M. Amina, W. J. Basirun, Appl. Surf. Sci., 2013, 283, 668–677.

[44] Z. Wu, L. Chen, C. Xing, D. Jiang, J. Xie, M. Chen, Dalton Trans., 2013, 42, 12980–12988.

[45] A. Daya Mani, P. Ghosal, Ch. Subrahmanyam, RSC Adv., 2014, 4, 23292–23298.

[46] Z. Khan, T. R. Chetia, A. K. Vardhaman, B. Dipankar, C. V. Sastri, Q. Mohammad, RSC Adv., 2012, 2, 12122–12128.

[47] Q. Yuan, L. Chen, M. Xiong, J. He, S. L. Luo, C. T. Au, S. F.Yin, Chem. Eng. J., 2014, 255, 394–402.

RSC Advances Accepted Manuscript